Semicond. Sci. Technol. 6 (1991) 862–871. Printed in the UK

# Five-valley model for the study of electron transport properties at very high electric fields in GaAs

**T González Sánchez, J E Velázquez Pérez, P M Gutiérrez Conde and D Pardo Collantes**

Departamento de Física Aplicada, Facultad de Ciencias, Universidad de Salamanca, 37008 Salamanca, Spain

Received 28 January 1991, accepted for publication 2 April 1991

**Abstract.** A Monte-Carlo method has been developed for the study of electron transport properties (drift velocity, average energy, electron ionization coefficient, etc.) in GaAs for high fields (100–600 kV cm$^{-1}$), using a five-valley conduction band model. To the three valleys traditionally used ($\Gamma_6$, $L_6$, $X_6$) two others have been added ($X_7$, $\Gamma_7$) that belong to conduction subbands above the first one. The model is shown to be also valid for the study of transport when a low electric field is applied (0–100 kV cm$^{-1}$). The results highlight the importance of the $X_7$ valley of the second conduction subband in high field transport phenomena, and are compared with different experimental values.

## 1. Introduction

The application of the Monte-Carlo method to the study of GaAs transport properties has been considerably improved since its introduction in 1966 [1], searching for a model that could describe its characteristics within the range of the electric field in which it is used. This interest is due to the possibility of constructing GaAs electronic devices that can operate at very high frequencies.

The working of many of these GaAs electronic devices is based on high-energy (hot) electrons. Impact ionization is a basic mechanism in the operation of certain devices, such as photodetectors and Impatt diodes. The models should also characterize these phenomena.

It is thus necessary to establish models which can describe GaAs transport properties from low to very high (500–600 kV cm$^{-1}$) electric fields. The Monte-Carlo method is valid for simulating the GaAs response in this wide range of electric field variation. If this method is employed not only to study the GaAs transport properties but also for the simulation of devices built with this semiconductor, the models used should reach a compromise between simplicity (in order to decrease calculation time as much as possible) and the validity of their results.

When Aspnes [2] stated the correct ordering of the valleys in the first GaAs conduction subband, different research groups began to carry out Monte-Carlo simulations with this ordering to study electron transport phenomena. Until that time a conduction band of only two valleys had been used.

Several authors [3–5] carried out simulations for low fields (lower than 100 kV cm$^{-1}$) using an analytical model for the conduction band formed by three spherical non-parabolic valleys. They achieved a good fit with the experimental results. Some of the parameters used in the simulations were initially taken as adjustable, with the aim of reaching an agreement with the experimental results for drift velocity.

Pearsall *et al* [6] found experimentally that the electron ionization coefficient depends on the electric field orientation, and thus on the band structure. This dependence led several authors [7–10] to search for more sophisticated models for the conduction band, that would take into account the existing anisotropies. These authors used a band structure calculated by the pseudopotential method for the analysis of the GaAs transport processes at high fields. They adopted the equation obtained by Keldysh [11] for the ionization probability, with different values of threshold energy. Their results are consistent with the experimental ones, except for the anisotropy found by Pearsall *et al* [6] for the ionization coefficient.

The study of the ionization threshold energy dependence on the wavevector direction of the ionizing electron is also important in high field transport phenomena. Several authors have developed studies directed towards the determination of this threshold energy [13–15] using

0268-1242/91/090862+10 $03.50 

as a basis the graphic method developed by Anderson and Crowell [12], which requires a detailed knowledge of band structure. Beattie *et al* [14], using bands calculated by the $\boldsymbol{k} \cdot \boldsymbol{p}$ method, and Sano *et al* [15], with bands calculated by pseudo-potential methods, were able to determine threshold energy surfaces in the wavevector space. In both cases they found that the threshold energy surface for GaAs do not vary too much with the wavevector orientation.

The present paper describes a Monte-Carlo method for the study of transport phenomena in GaAs. Although it was primarily developed to study processes at high fields, it provides good results for both low and high fields. The main novelty introduced here is the inclusion of two new upper valleys ($X_7$, and a fictitious valley we call $\Gamma_7$* that represents the influence of the $\Gamma_7$ and $\Gamma_8$ valleys), which together with the three ones traditionally used ($\Gamma_6$, $L_6$, $X_6$) constitute the conduction band.

The high energies reached by the carriers in the three lower valleys when they are subjected to very high fields (100–600 kV cm$^{-1}$) permit their promotion to higher valleys beyond the first conduction subband. These valleys play a very important role in transport phenomena at high fields, as will be seen in the case of the $X_7$ valley.

The present work aims to find a relatively simple model to characterize the behaviour of GaAs subjected to the action of high electric fields. This model has been developed for its use in the simulation, with a multiparticle Monte-Carlo method, of electronic devices made of this material (Impatt diodes, photodetectors). Such simplicity should result in a maximum saving of computation time. This is the main reason for adopting a simple analytical equation for the valleys of the conduction band: non-parabolic spherical valleys. The model does not describe exactly the shape of the conduction band for high energies, but the inclusion of the higher valleys ($X_7$, $\Gamma_7^*$) makes it possible to obtain results close to the experimental ones. We also adopt a simple model for the ionization processes, consistent with the isotropic character of the bands employed; in spite of its simplicity, it fits the experimental results [16] fairly well.

We have obtained results for both low and high fields. The former were compared with the experimental ones for drift velocity obtained by several authors [17–20], and were found to fit them. This fit was expected, since the new valleys only have an effect when the carrier has high energy.

In the case of high fields, the results were also compared with the available experimental data on both velocity [20] and ionization coefficient [16], and were found to fit them adequately.

The simulation was carried out at several different temperatures: 160, 210, 250 and 300 K.

## 2. Model used

### 2.1. Monte-Carlo method

The Monte-Carlo method used in the present study is very similar to the one described by Jacoboni and Reggiani [21]. It is a three-dimensional simulation in which we follow the trajectory of a single carrier which moves in the wavevector space in a uniformly doped N-type semiconductor, in this case GaAs, subject to the action of a constant electric field. The material is assumed to be infinite in the three dimensions of space, or at least sufficiently large. Given that the process is homogeneous and stationary, simulation of a single carrier is sufficient, provided that the process consists of a large enough number of scattering mechanisms to be able to obtain results that can be extrapolated for all the carriers in the semiconductor.

Under these conditions the movement of the electron is a succession of scattering mechanisms and free flights under the action of the electric field. During these free flights the only effect of the environment on the carrier is to give it an effective mass. The free flight time is determined randomly according to the probability distribution associated with all the possible scattering mechanisms. The type of interaction that ends a free flight is also selected at random according to the probability of each mechanism.

The scattering mechanisms taken into consideration in our simulation are the following: intervalley, and non-polar optical, both assumed as isotropic; polar optical, acoustic, piezoelectric and interaction with ionized impurities, all of which are considered anisotropic. The mechanisms with non-polar optical phonons have an effect only in the valleys whose minimum is in the $\langle 111 \rangle$ direction, i.e. the $L_6$ valleys. The impurification of the GaAs considered is low enough ($10^{15}$ cm$^{-3}$) for carrier-carrier scattering to be negligible.

The expressions for the probability of the different scattering mechanisms were calculated in accordance with the analytical model adopted for the valleys, as will be explained below. The state of the carrier after the scattering mechanism and the mean values of the magnitudes required were determined as explained by Jacobini and Reggiani [21] for homogeneous and stationary cases.

### 2.2. Band structure and physical parameters

As mentioned in the introduction, the GaAs conduction band is considered here to be formed of five valleys. Three of them constitute the first conduction subband ($\Gamma_6$, $L_6$, $X_6$), and are used traditionally. The other two valleys that we have introduced in our simulation are the $X_7$ valley and a valley that we will term $\Gamma_7^*$, which represents the contribution of the $\Gamma_7$ and $\Gamma_8$ valleys.

All the valleys respond to the same analytical equation, corresponding to non-parabolic spherical valleys. This equation is:

$$\varepsilon(1 + \alpha_i \varepsilon) = \hbar^2 \boldsymbol{k}^2 / 2m_i^* \qquad (1)$$

where $\hbar$ is the Planck constant divided by $2\pi$, $\alpha_i$ the non-parabolicity coefficient of the $i$ valley, $m_i^*$ the effective mass at the bottom of the $i$ valley, $\varepsilon$ the kinetic energy of the electron, and $\boldsymbol{k}$ its wavevector.

The $\Gamma_6$, $L_6$ and $X_6$ valleys have a limit to the energy

that the electron can reach in them, which is not the case for the $X_7$ and $\Gamma_7^*$ valleys, in which the carrier can attain any amount of energy. This energy limit is established in the same way for the three valleys. From a first energy value, only those scattering probabilities corresponding to the intervalley mechanisms are different from zero, which means that the carrier must leave those valleys at the end of the free flight if it finishes the flight with an energy above that first limit. The value of that energy for the $\Gamma_6$, $L_6$ and $X_6$ valleys is 2.0, 1.06 and 2.07 eV, respectively, measured from the bottom of the $\Gamma_6$ valley. Moreover, a second energy value is established (0.25 eV above the former in each valley) so that no carrier can finish a free flight with an energy above the second limit. Should this occur, the free flight is rejected, and a random number produced again in order to determine its duration until the final energy of the flight does not exceed this second limit. Furthermore, the carrier is not allowed to descend from higher valleys to one of these valleys when the final energy of the intervalley mechanism is above the first limit.

Figure 1(*a*) shows a real complete GaAs conduction band structure [10, 22]. The limit values adopted for the $\Gamma_6$, $L_6$ and $X_6$ valleys are seen to be similar to those appearing in the figure. It can also be seen that the valleys above the first conduction subband whose energy minimum is lower are $X_7$, and $\Gamma_7$ and $\Gamma_8$. Moreover, very high energy values can be reached in these valleys.

In our model, we have included the $X_7$ valley, which will be of great importance in high field transport phenomena, and the $\Gamma_7^*$ valley, with the aim of including the effects of the $\Gamma_7$ and $\Gamma_8$ valleys. As stated above, both valleys are considered to have no energy limit. Figure 1(*b*) shows a representation of the model adopted for the band structure in our simulation.

Several Monte-Carlo simulations [3–5] have been developed with models of three non-parabolic valleys ($\Gamma_6$, $L_6$, $X_6$), with no energy limit, in order to study low field transport (up to 100 kV cm$^{-1}$) in GaAs. The results obtained with these models were satisfactory, and fitted the experimental results. The reason for introducing an energy limit for these three valleys in our model is that for high fields (above 70 kV cm$^{-1}$) we detected, in our simulations with three unlimited valleys, the presence of carriers with energies above the real limits of these valleys —energies at which they are no longer valid. This happens in spite of the fact that the carrier tends to rise to higher valleys when its energy increases.

When transport phenomena at very high fields (300–600 kV cm$^{-1}$) are studied (including carrier multiplication by ionization), the carriers acquire more than enough energy to rise to the $X_7$ valley of the second conduction subband, and sometimes (for very high fields above 400 kV cm$^{-1}$) even sufficient to reach $\Gamma_7$ and $\Gamma_8$ valleys. Moreover, when ionization models are established with threshold energy above or around 2.0 eV (as in our case), in three-valley models there exists the possibility that the carrier, in order to ionize, should reach energies at which those valleys are no longer valid. Thus, for example, a carrier could never ionize in an $L_6$ valley, since there it cannot reach kinetic energies above 0.7–0.8 eV. A similar process occurs in the $X_6$ valleys, whose kinetic energy limits are around 1.5–1.7 eV. This does not occur in $X_7$, $\Gamma_7$ and $\Gamma_8$ valleys, since their kinetic energy limit is well above 2.0 eV.

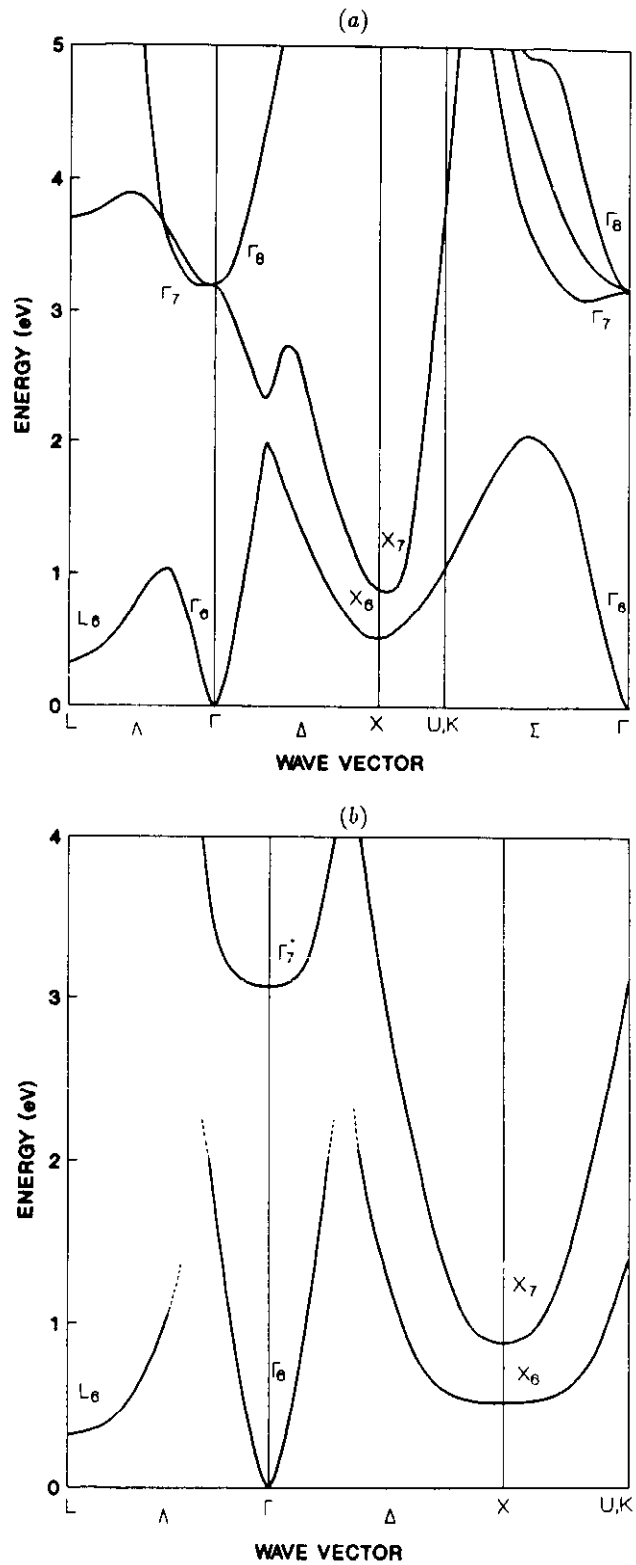


**Figure 1.** Conduction band structure for GaAs. (*a*) Complete [10, 22]. (*b*) Model used in the present simulation (vertical lines correspond to the energy between the two limits imposed in the $\Gamma_6$, $L_6$ and $X_6$ valleys).

Nevertheless, even though the carrier could reach these kinetic energy values in the first conduction subband, at such energies the probabilities of transition to higher valleys of other subbands cannot be ignored, and the carrier is likely to be in these higher valleys, as will be seen in our results.

For these reasons we introduce the $X_7$ and $\Gamma_7^*$ valleys, which are implemented with no energy limit, and which will play an important role in high field transport phenomena.

The model adopted has considerable limitations. An analytic model such as ours is fairly suitable for describing the bottom of the valleys, but when the energy in them increases, anisotropy increases and a spherical model such as the one proposed is not completely valid. Computation by pseudopotential methods of the complete band structure, as has already been done in models with three valleys [7–10], would be more adequate. With these computations, minima such as the one that appears in the second conduction subband in direction $\Delta$ could be considered.

However, upon introducing new valleys, the carriers move to the upper ones before they reach the higher energies in the lower ones, so that our band description becomes more accurate. Another factor which supports this statement is the fit obtained with the experimental results.

Furthermore, it is our intention to establish a simple model which is able to describe the behaviour of GaAs subjected to high electric fields, for its implementation in a two-dimensional simulator of devices [23] which work under these conditions (Impatt diodes, photodetectors, ...), where a more complex model would mean an excessive increase in computation time.

Table 1 shows the GaAs physical parameters used in the simulation. Those of the three lower valleys are similar to those generally calculated and accepted by several authors [22, 24] and which have already been used in previous simulations with three valleys [3–5]. The values of the intervalley coupling coefficients present the greatest discrepancies. We have adopted those established by Littlejohn *et al* [3], which provide a good fit to the experimental results [17–19] for low fields.

We had greater problems in determining the parameters characteristic of the higher valleys because of the scarcity of literature on this subject. The greatest difficulties were found with the $\Gamma_7^*$ valley, although because it has little effect on the final results (as will be seen) the fact that its parameters do not fit very well is not of great importance. Wang *et al* [25] studied parameters characteristic of the $X_7$ valley. From their results we have taken the values of the $X_7$ valley gap with respect to the bottom of the $\Gamma_6$ valley and its effective reduced mass. The gap of the $\Gamma_7^*$ valley with respect to the bottom of the $\Gamma_6$ valley is an intermediate value between the gaps of the $\Gamma_7$ and $\Gamma_8$ valleys given in the bibliography [24]. Some parameters,

**Table 1.** GaAs parameters used in the simulation.

| | |
|---|---|
| Density ($10^3$ kg m$^{-3}$) | 5.36 |
| Sound velocity ($10^3$ m s$^{-1}$) | 5.24 |
| Optical dielectric constant | 10.92 |
| Static dielectric constant | 12.90 |
| Piezoelectric constant (C m$^{-2}$) | 0.0565 |
| Ionized impurity concentration ($10^{15}$ cm$^{-3}$) | 1 |

| | Valley | | | | |
|---|---|---|---|---|---|
| | $\Gamma_6$ | $L_6$ | $X_6$ | $X_7$ | $\Gamma_7^*$ |
| Effective mass ($m^*/m_0$) | 0.063 | 0.222 | 0.58 | 0.25 | 0.35 |
| Non-parabolicity (eV$^{-1}$) | 0.7 | 0.5 | 0.3 | 0.8 | 0.7 |
| Energy separation (eV) (relative to $\Gamma_6$ valley) | 0.0 | 0.32 | 0.52 | 0.87 | 3.1 |
| Number of equivalent valleys | 1 | 4 | 3 | 3 | 1 |
| Acoustic deformation potential (eV) | 7 | 9.2 | 9.7 | 9.7 | 7 |
| Optical deformation potential ($10^{10}$ eV m$^{-1}$) | — | 3 | — | — | — |
| Intervalley deformation potential ($10^{10}$ eV m$^{-1}$): | | | | | |
| from $\Gamma_6$ | — | 10 | 10 | 8 | — |
| from $L_6$ | 10 | 10 | 5 | 10 | — |
| from $X_6$ | 10 | 5 | 7 | 10 | — |
| from $X_7$ | 8 | 10 | 10 | 10 | 10 |
| from $\Gamma_7^*$ | — | — | — | 10 | — |
| Polar optical phonon energy (eV) | 0.03613 | 0.03613 | 0.03613 | 0.03613 | 0.03613 |
| Non-polar optical phonon energy (eV) | — | 0.03430 | — | — | — |
| Intervalley phonon energy (eV): | | | | | |
| from $\Gamma_6$ | — | 0.0278 | 0.0299 | 0.0299 | — |
| from $L_6$ | 0.0278 | 0.0290 | 0.0293 | 0.0293 | — |
| from $X_6$ | 0.0299 | 0.0293 | 0.0299 | 0.0299 | — |
| from $X_7$ | 0.0299 | 0.0293 | 0.0299 | 0.0299 | 0.0299 |
| from $\Gamma_7^*$ | — | — | — | 0.0299 | — |

especially the intervalley deformation potentials, were determined to fit our results to the experimental ones [16, 20].

### 2.3. Impact ionization model

The model that we have developed for the calculation of the electron ionization coefficient is simple and requires little computation time. We establish a threshold energy, from which ionizations are produced, using a mixture of hard and soft threshold.

At the end of the free flight, the scattering mechanism taking place is chosen at random. If this scattering mechanism is an interaction with the lattice, then the ionization probability for the initial electron is:

$$W(\varepsilon) = U(\varepsilon - \varepsilon_{th}) \qquad (2)$$

where $\varepsilon_{th}$ is the threshold energy, $\varepsilon$ is the electron kinetic energy, and $U(x)$ is the unit step function: $U(x) = 1$ for $x \geqslant 0$ and $U(x) = 0$ for $x < 0$. If another type of mechanism (interaction with ionized impurities) takes place, the ionization probability is null.

Our threshold energy is clearly hard according to equation (2). However, it also has a soft character since the carrier does not ionize exactly when it reaches the threshold energy, but rather does so with the final energy of the free flight in which this threshold has been reached, which could be above the threshold energy.

When ionization occurs, the threshold energy is subtracted from the energy of the ionizing carrier, with which conservation of energy is assured. The value adopted for the threshold is 2.2 eV, which will be justified below. Given the GaAs band structure, in which no carrier in the $L_6$ and $X_6$ valleys can reach a critical kinetic energy above 2.2 eV, all the ionizations must occur in the $\Gamma_6$, $X_7$ and $\Gamma_7^*$ valleys. They occur especially in $X_7$, as will be seen.

The latest studies carried out by Beattie *et al* [14] and Sano *et al* [15] investigate the anisotropy shown by the threshold energy with the wavevector orientation, and determine threshold energy surfaces in the wavevector space. In both cases they find that for GaAs these surfaces do not present strong variations. Beattie *et al* [14] obtain threshold energy values for electrons contained between 2.15 and 2.35 eV. Sano *et al* [15], integrating the ionization probability (depending on the energy and the wavevector direction of the ionizing electron) to the first four conduction subbands in GaAs, obtain an ionization probability depending on the energy as shown in figure 2. This figure also shows the probability adopted by us. As can be seen, the values obtained by Sano *et al* [15] give an ionization probability which is close to a hard threshold such as ours. In the case of Si, a hard threshold such as the one used by us would be unacceptable, since the ionization probability increases much more slowly.

For these reasons, together with the need to find a simple model which requires little computation time, and the good fit of the model to the experimental results, we have adopted an isotropic hard threshold of 2.2 eV.

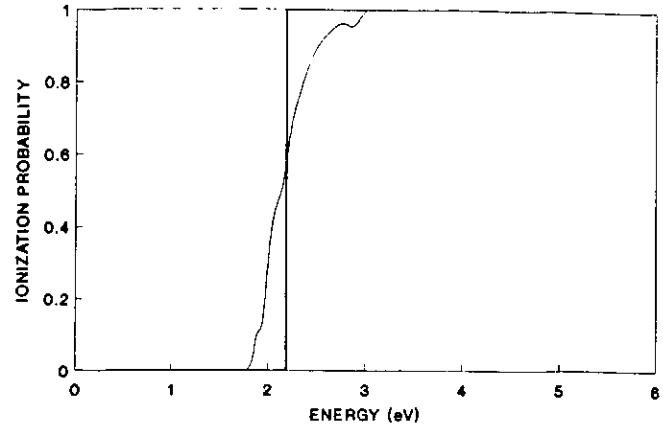


**Figure 2.** Ionization probability as a function of initiating electron energy: (—) obtained by Sano *et al* [15]; (—) our model.

Moreover, given the isotropic character of the bands used, it would not make much sense to establish an anisotropic ionization model.

## 3. Results for low fields

In this section, some of the results obtained for low electric fields (0–100 kV cm$^{-1}$) are presented. These results show that our simulation, although developed for the study of high field transport phenomena (100–600 kV cm$^{-1}$), also provides good results at low fields. Only the values obtained in the ⟨100⟩ direction are given, since they are the same as those obtained when the field is applied in the ⟨111⟩ direction.

The values obtained for the average drift velocity are shown in figure 3(*a*), together with various other experimental results [17–20]. The results obtained fit the experimental ones well, with a slightly higher value for fields between 10 and 100 kV cm$^{-1}$, values at which the carrier reaches high energies in the valleys, and anisotropy effects not considered in our isotropic model occur. Figure 3(*b*) shows the variation of this characteristic with temperature.

Figure 4 shows the results obtained for the average kinetic energy of the carrier. Initially, it increases rapidly with the electric field, due to the high presence of carriers in the $\Gamma_6$ valley, whose effective mass is small. As the field increases, the carriers pass to upper valleys with higher mass, which, together with the rise in the number of isotropic mechanisms produced, causes the increase in energy with the field to be much smaller.

As can be seen, in all the results the two higher valleys that we have introduced in the simulation have no effect, since carriers are not present in them.

## 4. Results for high fields

The effects that the $X_7$ and $\Gamma_7^*$ valleys included in our model have on transport processes at high fields can be

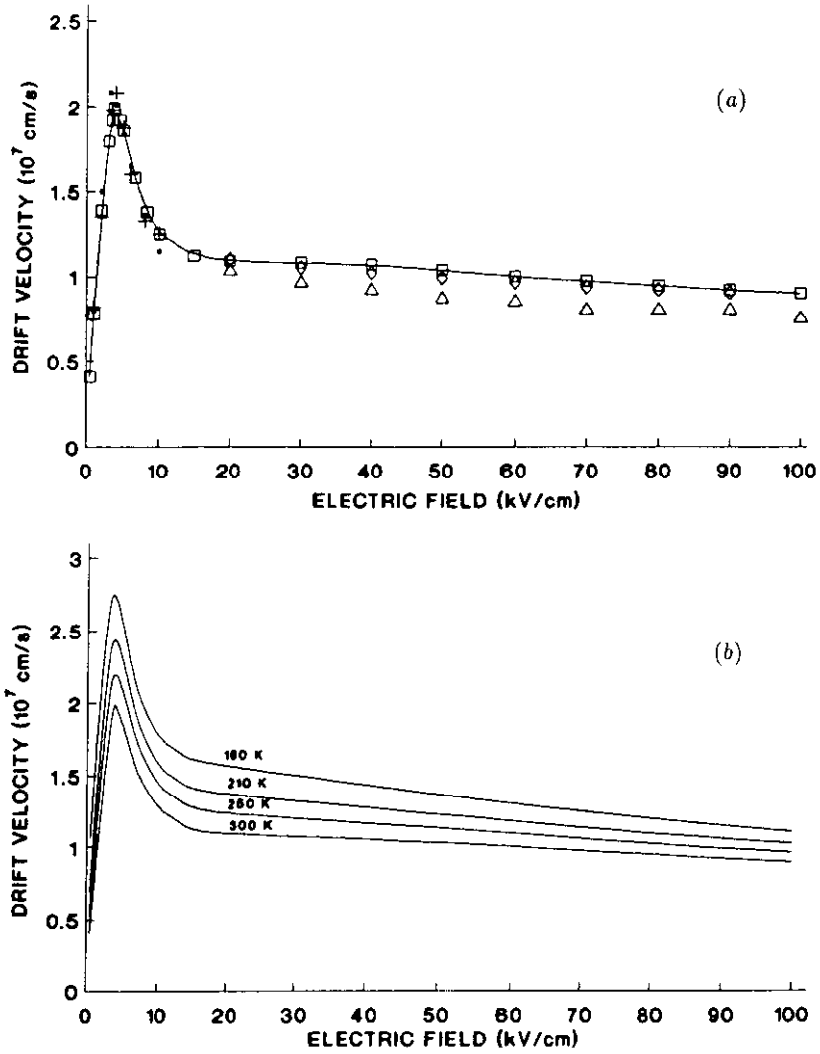


**Figure 3.** Average drift velocity as a function of electric field between 0 and 100 kV cm$^{-1}$. (*a*) Comparison with experimental results: ( • ) Ruch and Kino [17]; ( + ) Braslau and Hauge [18]; (◇) Riginos [19]; (△) Windhorn *et al* [20], (□) present results. (*b*) At several temperatures.

seen in figure 5(*a*). This figure shows the fraction of time that the carrier remains in each valley. It can be observed that at 70-80 kV cm$^{-1}$ some carriers have already reached enough energy to be in the $X_7$ valley, where the presence of electrons begins to be appreciable. The population of this valley increases considerably for higher fields, reaching 20% for field 300 kV cm$^{-1}$ and increasing to 40% for 600 kV cm$^{-1}$. This means that at very high electric fields (300-600 kV cm$^{-1}$) this valley will have a great influence on transport phenomena, together with the $X_6$ valley, which is even more populated than the $X_7$, although its occupation begins to decrease from 300 kV cm$^{-1}$.

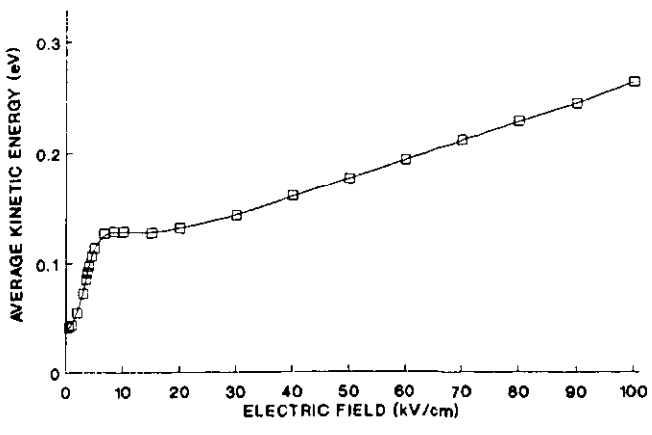


**Figure 4.** Average kinetic energy as a function of electric field between 0 and 100 kV cm$^{-1}$.

Nevertheless, the influence of the $\Gamma_7^*$ valley is minimal. Figure 5(*b*), whose scale is different from figure 5(*a*), shows the fraction of time that the carrier remains in this valley. Until they have reached fields above 250 kV cm$^{-1}$, the electrons do not attain enough energy to populate this valley. At 600 kV cm$^{-1}$, the electron remains in the $\Gamma_7^*$ valley only 0.016% of the total simulation time.

Figures 6(*a*), (*b*) and (*c*) show the distribution functions obtained for the different valleys for fields of 100, 300 and 500 kV cm$^{-1}$, respectively. In these figures it can be seen that as the field increases the carriers move to the higher valleys. Thus, the population of the $X_7$

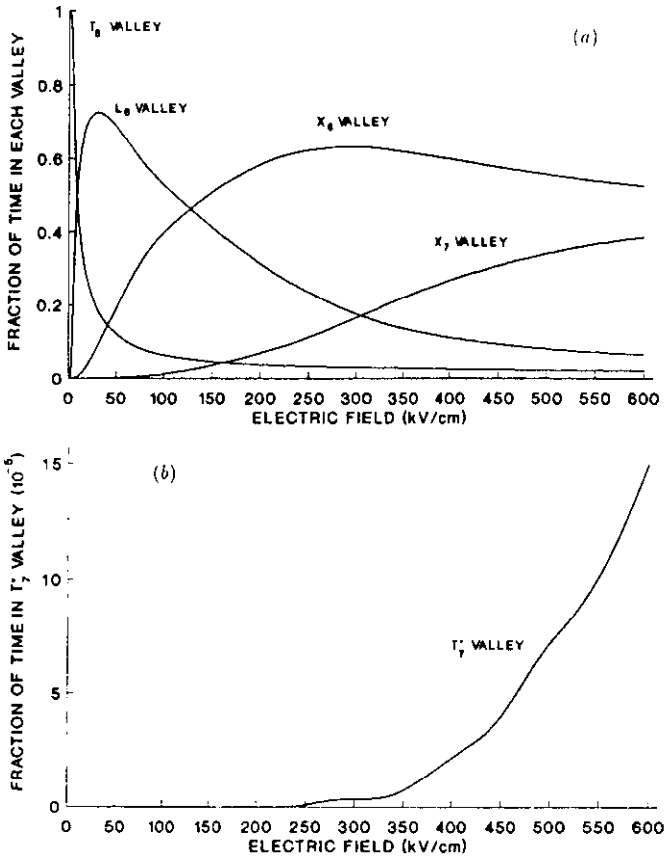


**Figure 5.** (*a*) Fraction of time the electron remains in each valley as a function of applied electric field. (*b*) Fraction of time the electron remains in the $\Gamma_7^*$ valley as a function of applied electric field.

valley steadily increases with the field, and the carriers concentrate in the $X_6$ valley at higher energies. These figures also show that it is practically only in the $X_7$ valley where carriers are present with a kinetic energy above 2.2 eV, the ionization threshold energy adopted. The presence of carriers in the $\Gamma_7^*$ valley is never enough for its distribution function to be significant.

The following results only include those obtained for fields applied in the ⟨100⟩ direction. Simulation was also developed for the ⟨111⟩ direction, but the results obtained were identical to those for the previous direction, as was to be expected given the isotropic character of the band model adopted. The results obtained for both directions are only given when there is a significant difference between them.

Figure 7(*a*) shows the values obtained for drift velocity together with the experimental ones of Windhorn *et al* [20]. It is observed that initially, for fields within the range 100–300 kV cm$^{-1}$, the velocity decreases slightly, since, in spite of the increase in the electric field, in that interval the carriers are still steadily increasing in population in the $X_6$ valley, which has an effective mass greater than that of the lower ones. However, above 300 kV cm$^{-1}$ the carriers begin to move to the $X_7$ valley in a great proportion, leaving the $X_6$ and $L_6$ valleys (Figure 5(*a*)). In the $X_7$ valley the effective mass is less than in the $X_6$ valley. This fact, together with the increase in the electric field, causes the drift velocity to increase with the field above 325 kV cm$^{-1}$, where a minimum appears. Thus, the $X_7$ valley plays an important role in this evolution.

In respect to drift velocity, only the experimental results of Windhorn *et al* [20] for the range 100–250 kV cm$^{-1}$ are available. Our results are slightly higher than these, in the same proportion as they were for low fields. This discrepancy, apart from being due to the effects of anisotropy in the bands that we do not consider, may also be due to the fact that the conditions of our simulation are ideal (boundless sample without traps, surface states, ...).

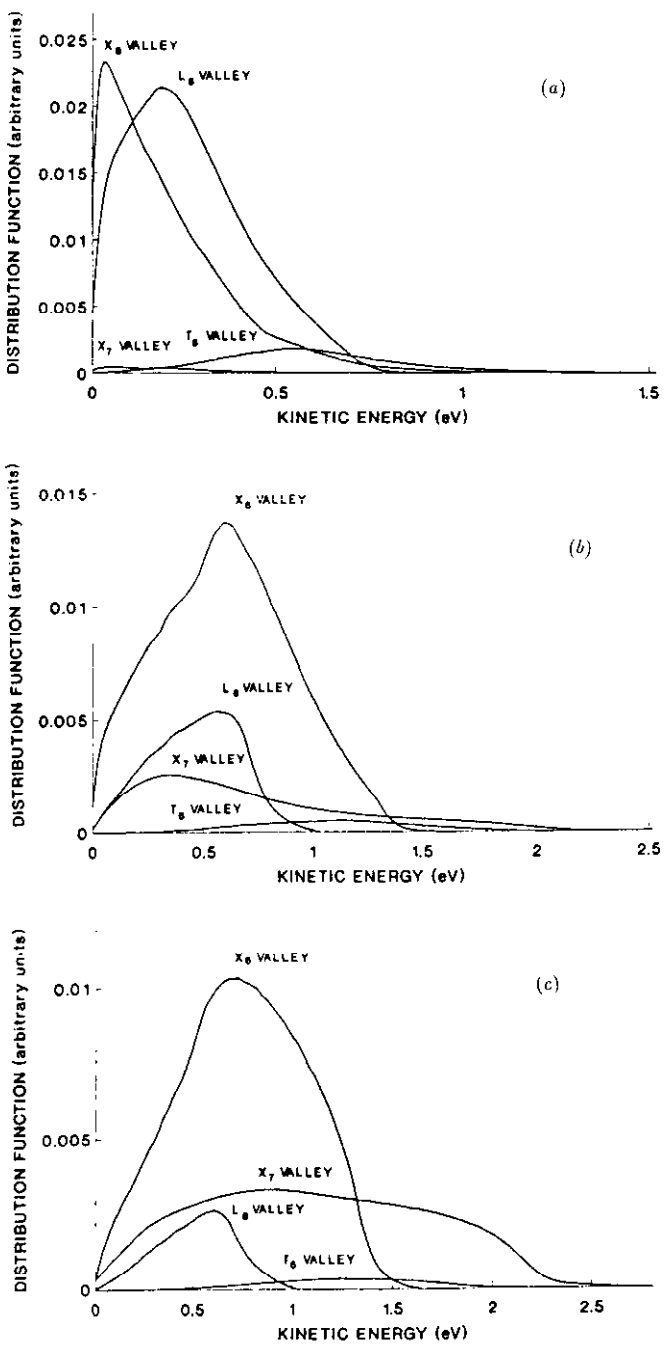


**Figure 6.** Electron distribution functions in each valley as a function of kinetic energy for an applied electric field of: (*a*) 100 kV cm$^{-1}$; (*b*) 300 kV cm$^{-1}$; (*c*) 500 kV cm$^{-1}$.

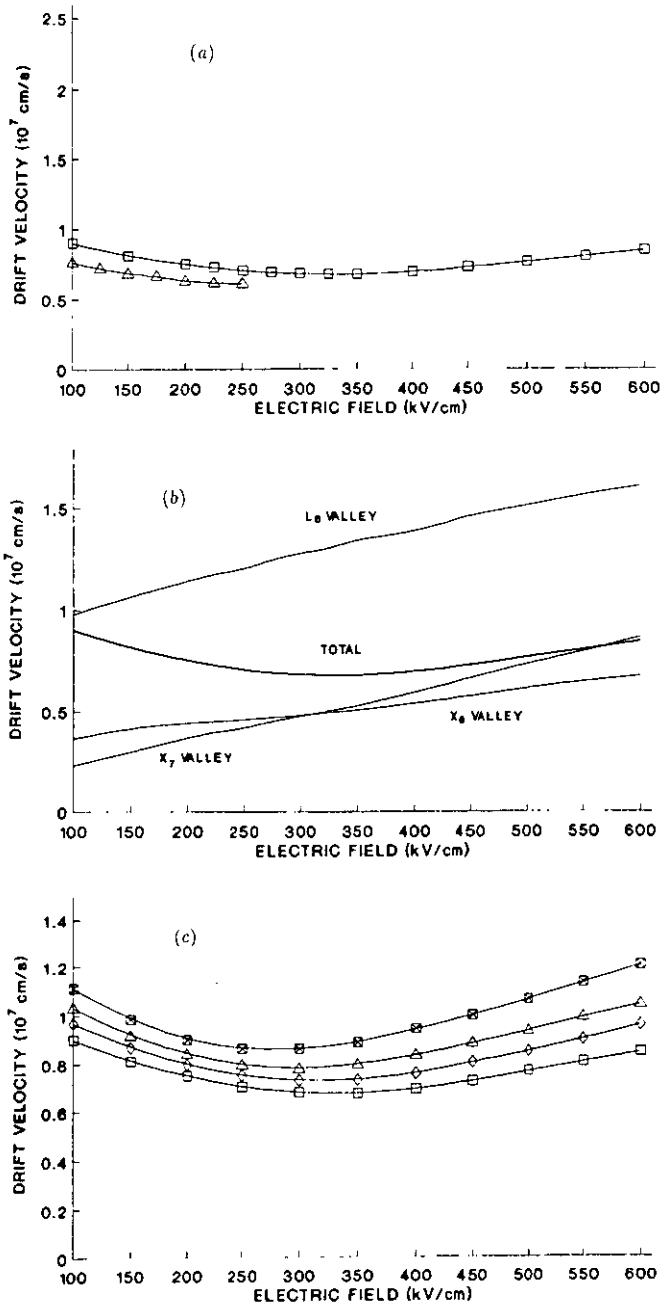


**Figure 7.** Average drift velocity as a function of electric field between 100 and 600 kV cm$^{-1}$. (*a*) Comparison with experimental results: (△) Windhorn *et al* [20], (□) present results. (*b*) In each valley. (*c*) At several temperatures: (⊠) 160 K, (△) 210 K, (◇) 250 K, (□) 300 K.

The average drift velocity in the three valleys that have most influence at high fields ($L_6$, $X_6$, $X_7$) is shown in Figure 7(*b*), where the velocity can be seen to increase progressively in the $X_7$ valley, surpassing that of the $X_6$ valley above 310 kV cm$^{-1}$. This causes the aforementioned increase in velocity when the $X_7$ valley is populated enough.

Figure 7(*c*) shows the average drift velocity as a function of field for various temperatures. It can be seen that the minimum of these characteristics is more pronounced and is produced for a lower value of applied electric field as the temperature decreases. This is due to

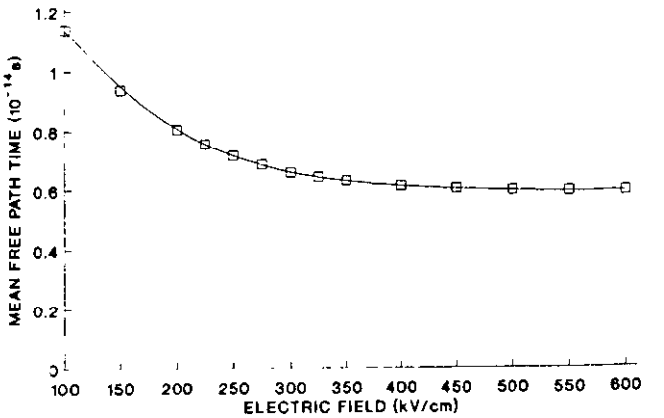


**Figure 8.** Mean free path time as a function of electric field.

the fact that the lower the temperature, the less the carriers interact with the lattice, undergoing longer free flights in which they gain more energy. Thus, they gain enough energy to move to the $X_7$ valley earlier, and populate it in greater quantity than at higher temperatures. These characteristics differ from the experimental ones in similar proportion to that observed for 300 K.

The average free flight time as a function of electric field (figure 8) shows a progressive decrease as the field increases, which is less marked at higher fields. The free flight time depends mainly on the total scattering probability, which for high fields is principally determined by the intervalley mechanisms, whose probability reaches a certain saturation at high energy, causing a drop in the slope of the free flight time characteristic for the higher fields. The introduction of the $X_7$ and $\Gamma_7^*$ valleys in the model has had scarcely any effect on this evolution.

The variations in drift velocity (figure 7(*a*)) and in free flight time (figure 8) cause the free flight to begin by decreasing, until it reaches a minimum value $0.42 \times 10^{-7}$ cm for 375 kV cm$^{-1}$, and to increase for higher fields due to the fact that the rise in drift velocity compensates the slight decrease in the free flight time.

Figure 9 shows the variation of the average kinetic energy with the electric field. Initially, it increases almost linearly with the field, to decrease its slope for fields

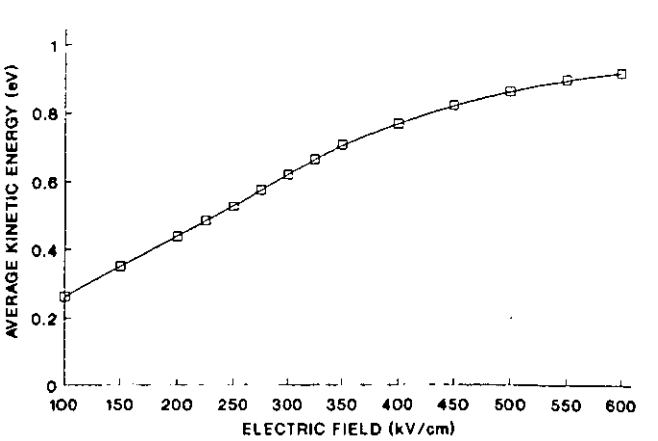


**Figure 9.** Average kinetic energy as a function of electric field between 100 and 600 kV cm$^{-1}$.

above 350 kV cm$^{-1}$. The inclusion of the $X_7$ valley means that in the transitions to this valley the carriers lose part of their kinetic energy in order to overcome the intervalley gap. Hence, when the field is very high and the carriers pass into the $X_7$ valley in large number, the increase in kinetic energy is less marked, in spite of the increase in the field and the stabilization of the free flight's duration. Also, the higher the field the greater the number of isotropic mechanisms (especially intervalley ones) produced, and these prevent the carrier from gaining much energy.

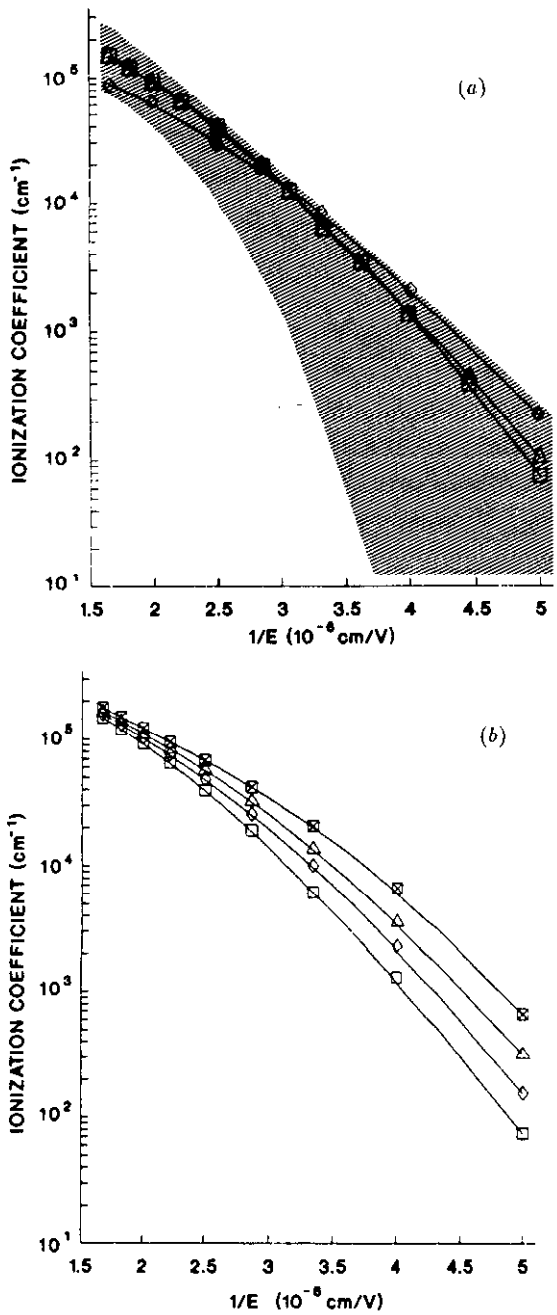


**Figure 10.** Electron impact ionization coefficient as a function of inverse electric field. (*a*) Comparison with experimental results: (◇) Bulman *et al* [16]; (□) present results for electric field applied in the ⟨100⟩ direction; (△) present results for electric field applied in the ⟨111⟩ direction (the shaded area represents the range of experimental results). (*b*) At several temperatures (⊠) 160 K, (△) 210 K; (◇) 250 K, (□) 300 K.

Figure 10(*a*) shows the electron ionization coefficient together with the experimental results of Bulman *et al* [16]. The shaded area corresponds to the range established for this parameter by the different experimental values [6, 16, 26-29]. In this case, we show the results obtained in our simulation for fields applied in the ⟨100⟩ and ⟨111⟩ directions, since there is a slight difference between them for low fields (200-250 kV cm$^{-1}$). Due to the small number of ionization processes that occur for these field values (from 5 to 15 for each million of scattering mechanisms), there is large statistical uncertainty in these results. This uncertainty can only be avoided by the use of a very long computation time. This source of mathematical error may be the cause of the discrepancy between our results and those of Bulman *et al* [16] for this range, and also for the difference between the values obtained for both directions. Hence, we cannot affirm that our model produces an anisotropic result (unexpected with the isotropic GaAs band structure adopted) for the electron ionization coefficient in this range.

As can be seen, our results are within the range established by the experimental ones, in the upper zone. Moreover, the dependence on the electric field is very similar to that obtained experimentally. Our results best fit the experimental results of Bulman *et al* [16], calculated in the ⟨100⟩ direction.

The effect of the $X_7$ valley on these processes is great, since, due to the GaAs band structure and the model proposed for the ionization processes (with a threshold of 2.2 eV), almost all the ionizations occur in this valley. This is due to the fact that the carrier never reaches that kinetic energy in the $L_6$ and $X_6$ valleys, and rarely in the $\Gamma_6$ valley, since before attaining it, it rises to a higher one, and in the $\Gamma_7^*$ valley it is very difficult for the carrier to reach such high energy. In our simulations, an ionization mechanism has only occurred sporadically in the $\Gamma_6$ valley, and so in the $\Gamma_7^*$ valley for very high fields.

The electron ionization coefficient against temperature is shown in figure 10(*b*). All of these characteristics are for a field applied in the ⟨100⟩ direction. As the temperature decreases, the interaction of the carriers with the lattice is smaller; the electron gains more energy in the free flights, and more ionization mechanisms occur. This is more marked for low fields in this range. When the fields are higher a similar number of ionization processes occurs for different temperatures in spite of the greater or lesser effect of the interactions with the lattice, due to the great magnitude of the field applied.

## 5. Conclusions

A simulation was carried out by means of the Monte-Carlo method in order to study electron transport properties at very high fields in GaAs, using for the conduction band a model formed by five non-parabolic spherical valleys. Three of these valleys form the first conduction subband ($\Gamma_6$, $L_6$, $X_6$) and have a limit in its

energy. The other two form part of the upper bands ($X_7$, $\Gamma_7^*$) and have no energy limit.

A simple model, consisting of an ionization probability with isotropic hard threshold energy of 2.2 eV, was implemented in order to determine the electron ionization coefficient. This type of model is possible due to the fact that the variation of the threshold energy with the wavevector direction of the ionizing carrier in GaAs is weak.

The validity of the model was also verified for low electric fields, and found to be in accordance with the experimental results for drift velocity.

Different results were obtained for high electric fields. The influence of the $X_7$ valley regarding transport phenomena in this range was found to be great, whereas the effect of the $\Gamma_7^*$ valley was practically negligible. The $X_7$ valley begins to be populated above 70-80 kV $cm^{-1}$, and 40% of the electrons occupy it when the field value is 600 kV $cm^{-1}$. The different results show the great influence of this valley at very high fields. The results for drift velocity are slightly higher than the experimental ones available, due to the ideality of the model. The results obtained for the electron ionization coefficient are in accordance with the range of the experimental results, with a dependence on the electric field that is very similar to some of them.

Given the isotropic character of the model adopted for the bands, in no case can we reliably show results which depend on the applied electric field orientation.

## Acknowledgment

This work has been supported by means of a collaboration agreement with IBM SAE.

## References

[1] Kurosawa T 1966 *Proc. Int. Conf. on the Physics of Semiconductors, Kyoto* (*J. Phys. Soc. Japan* suppl. A **49** 345)
[2] Aspnes D E 1976 *Phys. Rev.* B **14** 5331
[3] Littlejohn M A, Hauser J R and Glisson T H 1977 *J. Appl. Phys.* **48** 4587
[4] Kratzer S and Frey J 1978 *J. Appl. Phys.* **49** 4064
[5] Pozela J and Reklaitis A 1980 *Solid-State Electron.* **23** 927
[6] Pearsall T P, Nahory R E and Chelikowsky J R 1977 *Phys. Rev. Lett.* **39** 295
[7] Schichijo H and Hess K 1980 *Phys. Rev.* B **23** 4197
[8] Chang Y C, Ting D Z-Y, Tang J Y and Hess K 1983 *Appl. Phys. Lett.* **42** 76
[9] Brennan K and Hess K 1984 *Solid-State Electron.* **27** 347
[10] Fischetti M V and Laux S E 1988 *Phys. Rev.* B **38** 9721
[11] Keldysh L V 1965 *Sov. Phys. JETP* **10** 509
[12] Anderson C L and Crowell C R 1972 *Phys. Rev.* B **5** 2267
[13] Pearsall T P, Capasso F, Nahory R E, Pollack M A and Chelikowsky J R 1978 *Solid-State Electron.* **21** 297
[14] Beattie A R, Scharoch P and Abram R A 1989 *Semicond. Sci. Technol.* **4** 715
[15] Sano N, Aoki T and Yoshii A 1989 *Appl. Phys. Lett.* **55** 1418
[16] Bulman G E, Robbins V M and Stillman E 1985 *IEEE Trans. Electron Devices* **ED-32** 2454
[17] Ruch J G and Kino G S 1968 *Phys. Rev.* **174** 921
[18] Braslau N and Hauge P S 1970 *IEEE Trans. Electron Devices* **ED-17** 616
[19] Riginos V E 1974 *J. Appl. Phys.* **45** 2918
[20] Windhorn T H, Roth T J, Zinkiewicz L M, Gaddy O L and Stillman G E 1982 *Appl. Phys. Lett.* **40** 513
[21] Jacoboni C and Reggiani L 1983 *Rev. Mod. Phys.* **55** 645
[22] Shur M 1987 *GaAs Devices and Circuits* (New York: Plenum)
[23] Hesto P, Pone J F, Mouis M, Pelouard J L and Castagné R 1985 *Proc. 4th Int. Conf. on the Numerical Analysis and Integrated Circuits, NASECODE IV, Dublin* (Dublin: Boole)
[24] Landölt M and Börnstein J 1987 *Numerical Data and Functional Relationship in Science & Technology (New Series, Group III)* vol 22, subvol A (Berlin: Springer)
[25] Wang W B, Ockman N, Cavicchia M A and Alfano R R 1990 *Appl. Phys. Lett.* **57** 395
[26] Stillman G E, Wolfe C M, Rossi J A and Foyt A G 1974 *J. Appl. Phys.* **24** 471
[27] Ito M, Kagawa S, Kaneda T and Yamaoka T 1978 *J. Appl. Phys.* **49** 4607
[28] Ando H and Kanbe H 1981 *Solid-State Electron.* **24** 629
[29] Law H D and Lee C A 1978 *Solid-State Electron.* **21** 331